LA-UR-18-26056 (Accepted Manuscript)

Oxygen Effects on Solidification Behavior of Gas Tungsten Arc–Welded Laser Powder Bed Fusion–Fabricated 304L Stainless Steel

Gonzales, Devon Scott
Liu, Stephen
Javernick, Daniel Anthony
Pacheco, Robin Montoya
Brand, Michael J.
Johnson, Matthew Q.
Tung, David C.

To be published in: Materials Performance and Characterization

DOI to publisher's version: 10.1520/MPC20180115

Permalink to record: http://permalink.lanl.gov/object/view?what=info:lanl-repo/lareport/LA-UR-18-26056

Oxygen Effects on Solidification Behavior of Gas Tungsten Arc Welded Laser – Powder Bed Fusion Fabricated 304L Stainless Steel

Devon S. Gonzales[1], Stephen Liu[1], Daniel Javernick[2], Robin Montoya Pacheco[2], Michael Brand[2], Matthew Johnson[2], David Tung[2]

[1]Colorado School of Mines

[2]Los Alamos National Laboratory

Abstract

The laser – powder bed fusion (L-PBF) process inherently accumulates interstitial gas elements during powder fabrication and laser deposition processes. Such elements can lead to localized variations in the weld pool and affect the solidification behavior (when compared with its wrought equivalent), in addition to chemical micro-segregation within the fabricated material. This study was conducted to characterize the solidification behavior of gas tungsten arc welds made on L-PBF 304L stainless steel. The effect of surface active elements on the local solidification rates was studied. An emphasis was placed on the role local solidification rates and temperature gradients throughout the weld play on the resultant weld solidification structure and micro-segregation. It was determined that gas tungsten arc welds on L-PBF 304L stainless steel exhibited a vermicular ferrite solidification structure compared to a mix of vermicular and lathy ferrite structure in wrought 304L. The varying thermal gradients affected the solidification modes and partitioning of elements leading to fluctuations of micro-segregation in the L-PBF 304L. Macroscopically, such partitioning affected the surface tension within the weld pool, producing asymmetric weld pool geometries. The compositional differences between wrought and L-PBF fabricated 304L stainless steels resulted in irregular solidification behaviors during welding affecting the final weld microstructure.

Introduction

It is well established that the microstructural development of welds is directly related to composition and the solidification behavior of the molten metal. For a given stainless steel alloy, variations of minor elements have been shown to affect the morphology and stability of phases formed during solidification [1]. Such variability may also lead to increased susceptibility to weld cracking and failure [1-4]. Surface active elements such as sulfur and oxygen have been shown to affect welding characteristics of Type 304L stainless steel [5-8]. Sulfur precipitates low temperature sulfides which can lead to solidification cracking at grain boundaries [1,4]. Additionally, increasing sulfur content leads to changes in surface tension gradients in the liquid, changing bead morphology and increasing penetration [5,6]. Oxygen is an undesirable impurity

element as it can form insoluble oxides within the weld. The presence of deoxidizing elements in the alloy such and manganese and silicon precipitate low density oxides, creating silicate slag on the weld surface [9]. High oxygen concentration in the weld has been shown to behave similarly to sulfur in that surface tension gradients in the molten weld pool are affected, leading to higher penetration and modified weld geometries in Type 304L stainless steel [6]. Pollard showed that, besides oxygen, the addition of higher concentrations of manganese and silicon can also increase the penetration in gas tungsten arc welding of Type 304L stainless steel [7].

The solidification characteristics of the weld are related to the composition of the liquid, thermal properties and variables imposed by the process, such as heat input. Solidification behavior of Type 304L stainless steel is documented extensively in literature. Typically, solidification of the alloy is predicted by constitution diagrams developed for a wide range of compositions, comparing ferrite and austenite stabilizing elements. For Type 304L, solidification typically occurs as primary ferrite + austenite or primary austenite + ferrite, depending on the ratio of ferrite and austenite stabilizing elements, determined by calculations using constitution diagrams [2,10-14]. Studies have shown that changes in solidification rates and cooling rates can shift the solidification from primary ferrite to primary austenite, or vice versa, for a given composition [15-17].

Additive manufacturing is a relatively new fabrication process which is becoming more widely used commercially. Due to the relatively small build volume of powder bed fusion processes, large components or assemblies may need to be welded. Studies have shown that compositional and microstructural differences may be present in different regions of materials built via laser-powder bed fusion process compared to wrought alloys [18-20].

The current investigation compares the bulk and local compositional differences of wrought and laser-powder bed fusion fabricated Type 304L stainless steel to determine the effects of materials processing on weld solidification behavior of the alloy. Due to the inherent surface area of the powder used in the L-PBF process, the bulk concentration of oxygen is an order of magnitude higher than that of the wrought 304L alloy. The concentrations of manganese and silicon are also higher in the L-PBF material. To determine solidification behavior differences, autogenous gas tungsten arc welding was performed and solidification rates, cooling rates and temperature gradients were measured in the x, y, and z directions in the welds. The resultant solidification parameters were compared to compositional and microstructural differences observed in the welds.

Materials and Methods

Laser-powder bed fusion samples were produced using an EOS M280 machine using virgin 304L powder of bulk composition given in Table 1. Samples were built to dimensions 50 mm length (longitudinal direction), 25 mm height (build direction), and 3.5 mm thickness. A stress relief annealing heat treatment of 1065°C for 30 minutes, and air cooled, per AMS2759/4C

specification, was conducted on the L-PBF samples. The L-PBF samples were machined following heat treatment to 2 mm thickness. Hot rolled sheets of 2 mm thick 304L wrought alloy were cut to equivalent dimensions as the L-PBF specimens. Bulk compositions of wrought and post-heat treated and machined L-PBF specimens are detailed in Table 1.

Table 1. Compositions in weight percent of 304L powder, the L-PBF 304L build and wrought 304L base material; major differences in silicon, carbon, phosphorus and oxygen.

Element (wt%)	Fe	Cr	Ni	Mn	Si	C	S	P	N	O
Powder 304L	69.800	18.410	9.560	1.520	0.580	0.011	0.002	0.010	0.055	0.038
L - PBF 304L	69.562	18.563	9.565	1.468	0.709	0.014	0.003	0.013	0.049	0.032
Wrought 304L	71.121	18.111	8.012	1.747	0.271	0.049	0.001	0.031	0.072	0.002

All samples were gas tungsten arc welded using a Miller Dynasty 350 power supply and a computer numerical controlled (CNC) torch. Samples were clamped on both sides and welded perpendicular to the build direction for L-PBF as shown schematically in Figure 1. Welding was along the rolling direction for wrought material. Autogenous, partial penetration welds were generated using the two different weld schedules given in Table 2.

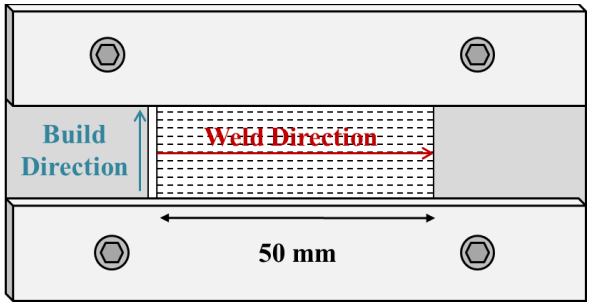

Figure 1. Schematic drawing of the fixture used during welding. Arrows indicate the orientation relationship of the welding direction with respect to build direction for L-PBF 304L samples.

Table 2. Weld schedule parameters for two heat inputs used in this investigation.

Weld Schedule	Shielding Gas	Flow Rate (cfh)	Pre/Post Flow Time (s)	Current (A)	Voltage (V)	Travel Speed (mm/s)	Arc Length (mm)	Efficiency (%)	Heat Input (J/mm)
WS - 8	**UHP - Ar**	**40**	**10/10**	**90**	**9.9**	**3.39**	**2**	**80**	**210**
WS - 10	**UHP - Ar**	**40**	**10/10**	**90**	**9.9**	**4.23**	**2**	**80**	**168**

Weld specimens were characterized through metallographic examination of top-view and side-view longitudinal cross sections along the centerline, and transverse cross sections taken at various locations along the weld to create a three-dimensional reconstruction of pool shape and solidification parameters within the weld. The effect of solidification rate, cooling rate and

temperature gradients within the weld pool were related to the solidification structure. Solidification rates were measured experimentally using the top-view longitudinal and side-view longitudinal method to measure dendrite growth angles through the thickness of the weld. By measuring the top-view growth angle of θ, and the side-view growth angle Φ (Figure 2), the true dendrite growth angle with respect to travel direction, α, is determined by the equation [21]:

$$tan\alpha = \sqrt{(tan\theta)^2 + (tan\Phi)^2}$$

The growth angle, α, can then be applied to the dendrite growth rate equation R = V *cos* α. Measurements were obtained from four regions through the depth of the weld. Solidification rates were determined from the average of ten measurements taken from three fields of view, per region, at the weld start, middle (steady-state), and end.

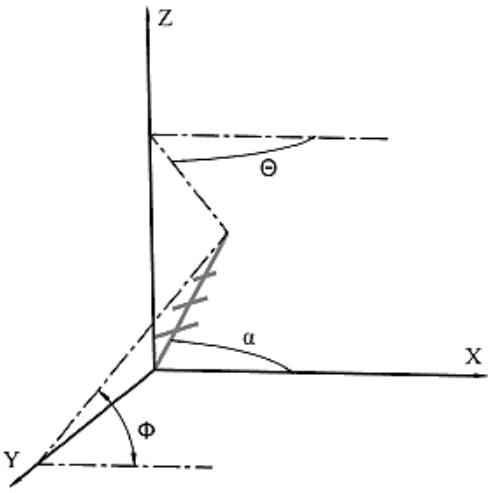

Figure 2. Schematic drawing of the true dendrite growth angle within a weld [21].

Cooling rates were measured experimentally using the dendrite arm spacing relationship $d=a(\varepsilon)^{-n}$ where d is the dendrite arm spacing (DAS), ε is the cooling rate, n is the slope of the linear relationship of *d* to *ε* and a is a proportional constant determined experimentally [14]. Katayama and Matsunawa determined the linear relationship as $d=80(\varepsilon)^{-0.33}$ for type 310 stainless steel and was applied to type 304 stainless steel [15]. It was assumed that this relationship was valid for approximating the cooling rates in the 304L alloys used in this investigation. Measurements were obtained from the transverse and longitudinal cross sections of the weld to determine spatial variations in the weld pool. The average of ten measurements was obtained in eight regions of the transverse cross-sections and the four regions used to determine solidification rate. Temperature gradients (G) within the weld pool were calculated using the relationship G = R/d. The solidification parameters determined in this investigation were related to microstructural analysis to characterize the solidification behavior of gas tungsten arc welds made on L-PBF 304L stainless steel.

Results and Discussion

Wrought 304L stainless steel alloy was acquired with specifications to match the composition of the L-PBF 304L as closely as possible. The oxygen content of both materials was varied to isolate the effects on the weld solidification behavior during gas tungsten arc welding and the resultant microstructure. The bulk oxygen concentration of the wrought 304L alloy contained 30 ppm oxygen compared to 320 ppm in the L-PBF 304L alloy. Locally, the concentration of oxygen varied significantly throughout the L-PBF base material with larger variability toward the top of the build (increasing build height) as compared with the bulk composition. The content of oxygen was related to differences in weld solidification behavior between the two base materials.

The undisturbed surfaces of the welds were inspected prior to cross sectioning to observe macroscopic differences in welding behavior between the wrought and L-PBF specimens. Figure 3 shows the contrasting responses under identical welding conditions. Figure 3a depicts the surface topography of a GTA weld on wrought 304L stainless steel showing a lack of surface oxidation and a planar surface. Using channeling contrast in the backscatter electron detector, the grain structure was revealed to be elongated and followed the direction of the heat source as in a typical weld. Figure 3b shows the surface topography of the L-PBF weld specimens largely different to that of its wrought counterpart. The bulk of the surface is free of oxidation, however, the toe-line of the weld is decorated with silicate islands (dark), with some extending into the weld as if they were drawn in by surface tension gradients generated by the solidifying weld pool. Additionally, channeling contrast demonstrates a more equiaxed grain structure within the weld. Such grain refinement is likely caused by the formation of silicates within the weld pool providing more sites for heterogeneous nucleation to occur, and subsequent rejection of the silicates to the weld surface.

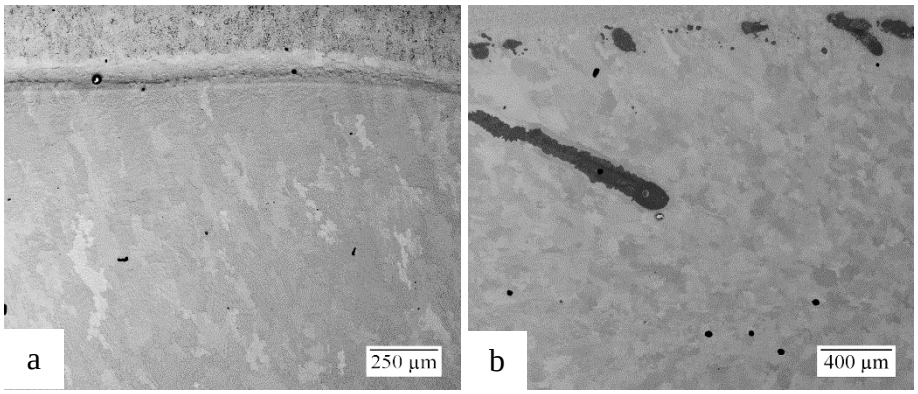

Figure 3. Backscattered electron images along the surface toe-line of a gas tungsten arc weld on a) wrought 304L, and b) L-PBF 304L using the WS-10 weld schedule.

Transverse cross sections were taken from the welded wrought and L-PBF specimens for geometric and microstructural characterization. Figure 4 displays the typical weld geometries produced from both weld schedules for wrought and L-PBF samples. The differences in weld penetration and geometry between both types of samples are visually evident and are corroborated by measured depth-to-width aspect ratios of 0.20, 0.14, 0.43, and 0.35 for Figures 4a through 4d, respectively. Such aspect ratios of the welds agree well with data published separately by Pollard and Roper on the effects of oxygen on the weld penetration in type 304L stainless steel [6,7]. It was also observed that in Figures 4c and 4d, there is asymmetry of the weld with respect to the centerline. In both cases the weld pool tends to extend to the right when viewed along the welding direction creating a bulge in the transverse direction. Such feature can be directly related to the build direction of the L-PBF base metal. Referencing Figures 4c and 4d, the left to right direction of the images corresponds to the bottom to top build direction of the L-PBF samples. WDS analysis of the L-PBF base material indicates there is a gradient of local oxygen concentration from 450 ppm within the bottom and 900 ppm within the top build layers. Such oxygen gradient is expected to be sufficient to affect the convective fluid flow of the weld and draw the weld pool toward the region of highest surface tension, creating an asymmetrical bead profile.

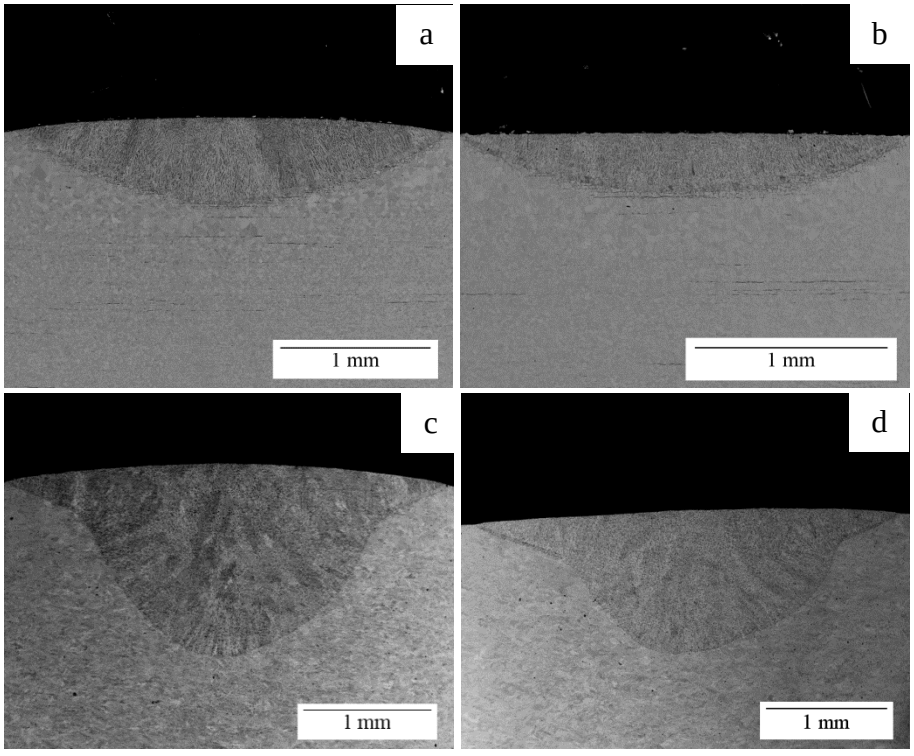

Figure 4. Backscattered electron images of the transverse cross sections for a) wrought 304L WS-8, b) wrought 304L WS-10, c) L-PBF 304L WS-8, and d) L-PBF 304L WS-10 gas tungsten arc welds.

Based on the compositions of the wrought and L-PBF 304L specimens, the chromium and nickel equivalencies were determined based on calculations from the WRC-1992 constitution diagram for stainless steels [22]. Such equivalencies can be used to predict the primary solidification sequence type and subsequent austenite and ferrite morphologies. The calculations determined WRC-1992 Cr_{eq}/Ni_{eq} ratios for the wrought and L-PBF specimens to be 1.64 and 1.68 respectively, which predicts type FA, or primary ferrite solidification sequence followed by austenite formation. The resultant ferrite morphology would be vermicular ferrite for moderate cooling rates and lathy ferrite for higher cooling rates [11]. Welds conducted on the wrought 304L specimens yielded similar microstructures, the difference being size of the solidification structure, which was attributed to the difference in heat input and subsequent cooling rates. The weld microstructure, shown in Figure 5, was primarily vermicular ferrite morphology with localized areas of lathy ferrite dispersed throughout. Ferrite + Widmanstätten austenite formed along the fusion line for both weld schedules. Due to the high temperature gradients and cooling rates experienced at the fusion line, it is likely that the mobility of ferrite stabilizers are restricted and pushed to the sides of the growing tips instead of piling up ahead of the planar front allowing the austenite to grow as Widmanstätten morphology. Figure 6 shows a schematic drawing relating solidification rates and composition to types of solidification microstructure within austenitic stainless steel welds. The hashed region highlights the composition range used in this investigation and the horizontal line delineates the maximum solidification rate measured. It is possible that due to high cooling rates and segregation of ferrite stabilizers, the local composition shifted such that Ferrite + Widmanstätten austenite became the favorable solidification mode at the fusion line.

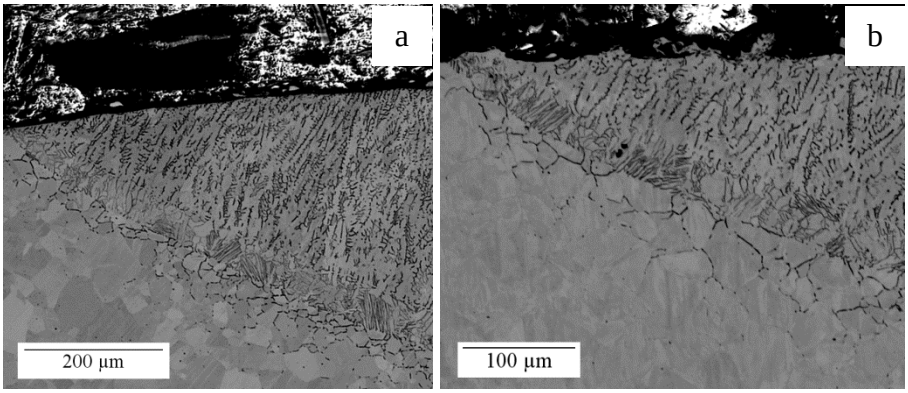

Figure 5. Backscattered electron cross section images showing the solidification structure of wrought 304L in welds produced via schedule a) WS-8, and b) WS-10.

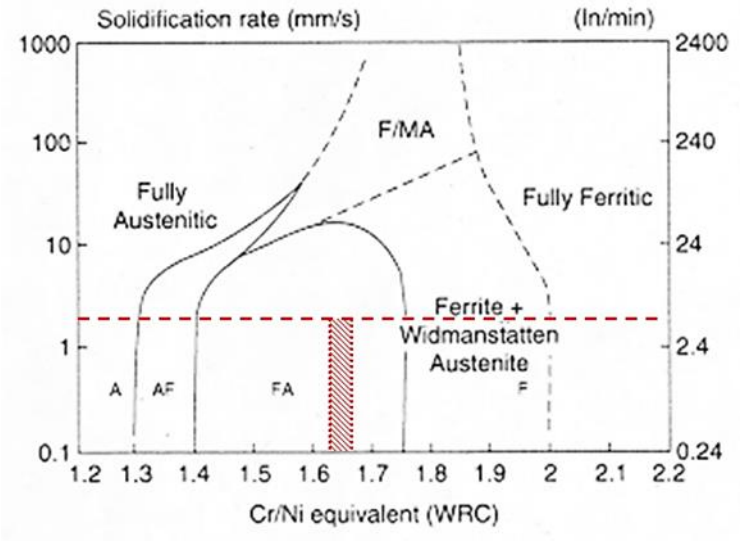

Figure 6. Schematic relating the effects of solidification rate and composition to the microstructure in welding of austenitic stainless steels [3].

The microstructure observed in the welded L-PBF specimens considerably differed from that of the wrought specimens. Figure 7 depicts various regions within the L-PBF welds that contrast observations made in the wrought 304L welds. Near the toe-line, in Figure 7a, the microstructure resembles that of the wrought specimens having a vermicular ferrite solidification morphology and Ferrite + Widmanstätten austenite constituting the fusion line morphology. However, the fusion line geometry of the L-PBF samples change dramatically with depth of penetration, and the Ferrite + Widmanstätten morphology is lost abruptly and a more cellular solidification structure exists, shown in Figure 7b. Additionally, within the center of the region of high penetration in the L-PBF welds, the primary solidification mode changes from ferrite to austenite, shown in Figure 7c. This phenomena is attributed to a diffusionless transformation of ferrite to austenite at high solidification rates and cooling rates.

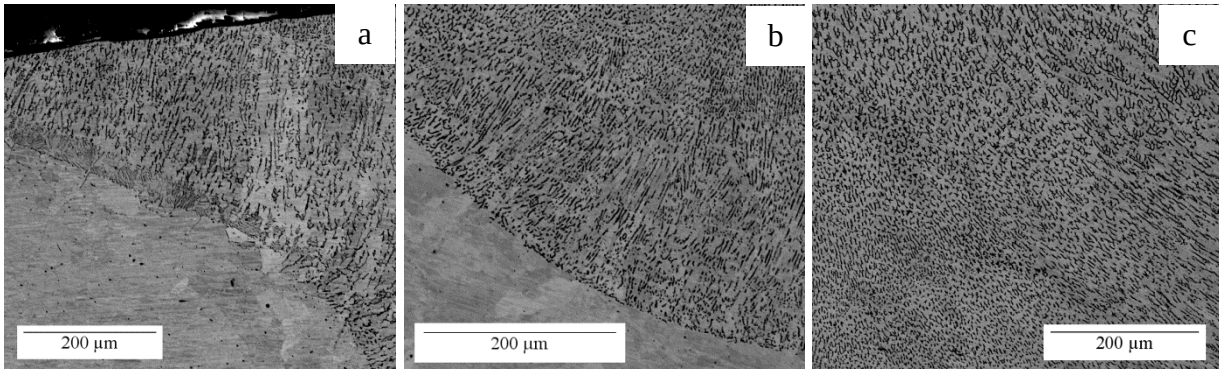

Figure 7. Backscattered electron cross section images showing the solidification structure of L-PBF 304L welds produced via schedule WS-10 a) near the toe, b) root, and c) central-right ‘bulge’ regions of the weld.

Characterization of longitudinal cross sections was used to validate observations made at the surface and within transverse cross sections. Figures 8a through 8d show examples of the steady-state longitudinal cross section along the centerline within the welds. The images given in Figures 8a and 8b are of wrought 304L specimens produced by weld schedules WS-8 and WS-10, respectively. With the exception of penetration depth, both schedules produced comparable welds having a consistent weld root and dendrite growth following the direction of heat extraction, or the heat source. Contrarily, L-PBF samples produced by weld schedules WS-8 and WS-10, in Figures 8c and 8d respectively, show a large modulation in penetration depth. The irregularity in penetration can be attributed to local variations in oxygen content of the base material. Additionally, the growth direction of the dendrites, and consequently solidification rate, changes periodically with respect to depth of the weld. This phenomenon is likely caused by the irregular weld bead shape, both longitudinally and transversely, creating eddy current flows and changes in fluid flow and heat extraction.

Measurements of solidification rate, cooling rate and temperature gradient variations were conducted three-dimensionally within the weld pool in an effort to relate microstructural and compositional variations to solidification parameters. Figure 9 shows schematically the regions which the welds were divided into longitudinal and transverse sections to measure the solidification parameters. It should be noted that L1, L2, L3, and L4 correspond to the centerline of T2, T5, T7 and T8, respectively. It is also important to note that L3 and T7 are analogous to the region of the L-PBF samples depicted in Figure 7c.

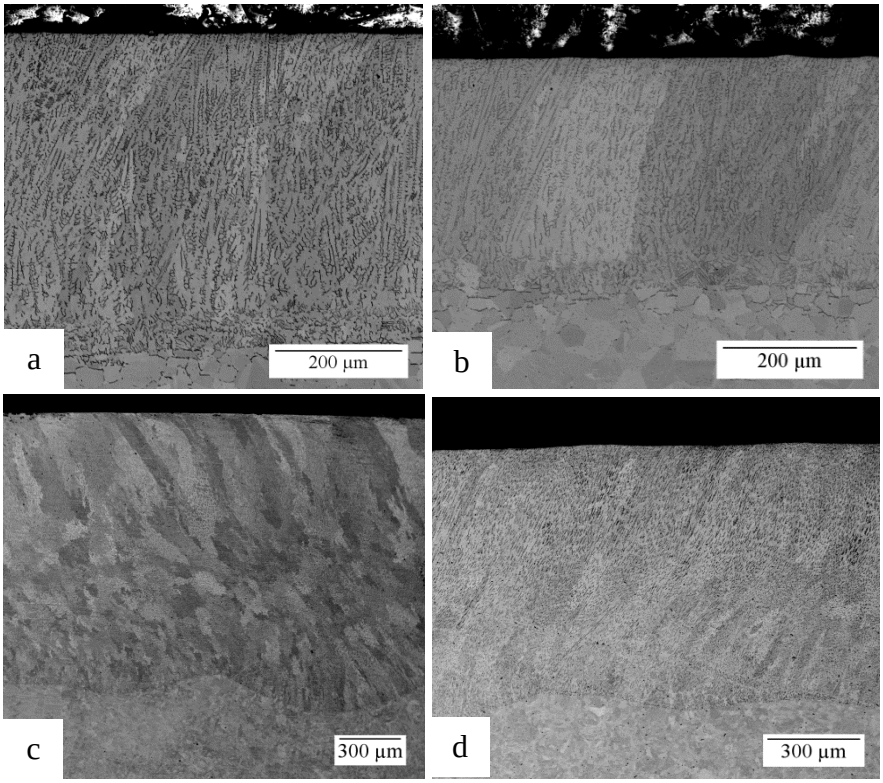

Figure 8. Backscattered electron images of the longitudinal cross sections for a) wrought 304L WS-8, b) wrought 304L WS-10, c) L-PBF 304L WS-8, and d) L-PBF 304L WS-10 gas tungsten arc welds.

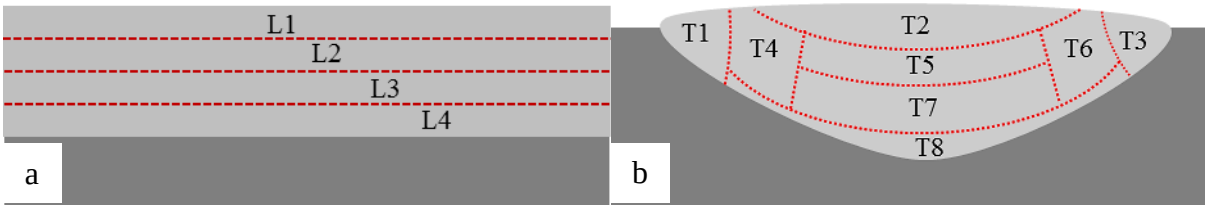

Figure 9. Schematic drawings of regions used to measure solidification parameters of the welds. a) Regions designated for longitudinal cross sections, b) regions designated for transverse cross sections.

Through-thickness solidification rates were measured using the two-angle method [21] (top-view and side-view) longitudinally along the length of the weld. The average solidification rates remained consistent along the length and the data acquired from the steady-state regions of the wrought and L-PBF samples is plotted for WS-8 and WS-10 in Figure 10a and 10b, respectively. Under both conditions, trends remain the same. Wrought 304L shows typical behavior for solidification of gas tungsten arc welds, where the solidification rate is a maximum at the surface and minimum and the fusion line. In the case of L-PBF, the solidification rate is

much faster than that of its wrought counterpart and in addition, the growth rate increases sharply above the fusion line, then decreases and begins to behave normally.

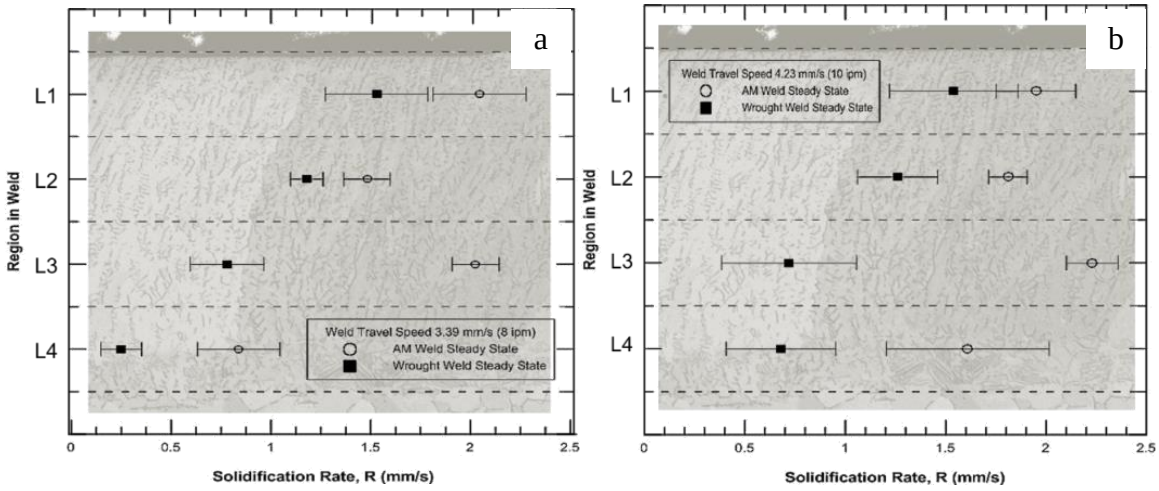

Figure 10. Solidification rate data as a function of depth in the weld along the longitudinally cross section for a) WS-8, and b) WS-10.

The average measured cooling rates, solidification rates and temperature gradients for each region analyzed in wrought and L-PBF samples generated by schedule WS-8 in Table 3 and samples generated by schedule WS-10 are given in Table 4. Dissecting Table 3 and Table 4 it can be seen that the trends remain constant only differing in values due to heat input. Near the top and middle of the welds, namely T1 through T6, L1 and L2, the cooling rates and temperature gradients of both the L-PBF and wrought samples are nearly identical and the solidification rate following the same model at different speeds. The major discrepancies lie within the regions T7, T8, L3 and L4. The cooling rate is significantly high in T7 (L3), coupled with a higher solidification rate such that it may be possible to shift the primary solidification mode to austenite, justifying the presence of microstructural observations made from Figure 7c. It is also apparent that in T8 (L4), the cooling rates and temperature gradients are extremely high in the wrought samples, fostering the conditions needed to produce Widmanstätten austenite, which was found in Figure 5. The temperature gradients are significantly lower in the root of the L-PBF welds reducing the likelihood of Widmanstätten austenite growth, exemplified in Figure 7b.

It has been shown by previous researchers that increasing oxygen concentration in 304L stainless steel has a significant effect on weld penetration and fluid flow of the weld pool. The current investigation determined that L-PBF 304L stainless steel sheet contains gradients and irregular variations in oxygen concentration, thus leading to unstable fluid flow and subsequent solidification behavior.

Table 3. Solidification parameter data for GTA weld on L-PBF and wrought 304L using weld schedule WS-8.

Weld Schedule WS-8						
L-PBF 304L						
Region	**ε (°C/s)**	**Δε (°C/s)**	**R (mm/s)**	**ΔR (mm/s)**	**G (°C/mm)**	**ΔG (°C/mm)**
T1	1193.4	513.4	1.89	0.12	631.4	271.6
T2	3725.5	980.6	2.05	0.23	1817.3	478.3
T3	1603.6	491.3	1.89	0.12	848.4	259.9
T4	752.5	212.9	1.41	0.08	533.7	151.0
T5	1468.5	804.2	1.48	0.12	992.2	543.3
T6	1242.2	530.1	1.41	0.08	881.0	376.0
T7	4244.7	1641.3	2.03	0.12	2091.0	788.1
T8	2641.1	1483.6	0.84	0.21	3144.1	1766.2
L1	2892.5	463.8	2.05	0.23	1410.9	285.3
L2	1167.2	329.5	1.48	0.12	788.7	203.5
L3	2659.3	378.1	2.03	0.12	1310.0	256.4
L4	3731.0	509.6	0.84	0.21	4441.7	416.7
Wrought 304L						
Region	**ε (°C/s)**	**Δε (°C/s)**	**R (mm/s)**	**ΔR (mm/s)**	**G (°C/mm)**	**ΔG (°C/mm)**
T1	734.2	270.2	1.25	0.32	587.4	216.2
T2	2990.2	1139.4	1.52	0.55	1954.4	744.7
T3	726.5	300.2	1.25	0.32	581.2	240.2
T4	634.3	349.5	0.88	0.18	720.8	397.1
T5	1079.9	317.6	1.18	0.08	915.2	269.2
T6	672.3	324.1	0.88	0.18	764.0	368.2
T7	754.9	314.1	0.78	0.28	967.8	392.4
T8	2450.1	503.1	0.25	0.11	9800.4	2012.2
L1	2041.2	223.1	1.53	0.55	1334.1	145.8
L2	1062.1	236.8	1.18	0.08	900.1	200.7
L3	631.2	74.5	0.78	0.28	809.3	95.6
L4	1910.7	274.4	0.25	0.11	7643.0	1097.7

Table 3. Solidification parameter data for GTA weld on L-PBF and wrought 304L using weld schedule WS-10.

Weld Schedule: WS-10						
L-PBF 304L						
Region	**ε (°C/s)**	**Δε (°C/s)**	**R (mm/s)**	**ΔR (mm/s)**	**G (°C/mm)**	**ΔG (°C/mm)**
T1	1704.4	398.5	1.42	0.14	1200.3	280.7
T2	3242.9	820.4	1.95	0.19	1663.0	420.7
T3	1090.4	525.6	1.42	0.14	769.2	370.8
T4	1033.2	515.3	1.63	0.18	633.9	316.1
T5	1837.3	601.4	1.81	0.09	1031.6	332.3
T6	1659.0	564.1	1.63	0.18	916.6	311.6
T7	3725.7	1279.7	2.23	0.13	1670.7	559.3
T8	2903.4	757.0	1.61	0.41	1803.4	470.2
L1	2344.2	475.3	1.95	0.19	1202.2	243.7
L2	817.1	110.9	1.81	0.09	451.8	61.2
L3	1697.7	229.7	2.23	0.13	761.3	103.0
L4	4387.9	541.4	1.61	0.41	2725.4	336.3
Wrought 304L						
Region	**ε (°C/s)**	**Δε (°C/s)**	**R (mm/s)**	**ΔR (mm/s)**	**G (°C/mm)**	**ΔG (°C/mm)**
T1	821.1	415.3	1.42	0.55	578.2	292.5
T2	2316.7	566.4	1.54	0.32	1504.4	367.8
T3	1084.4	241.3	1.42	0.55	763.7	169.9
T4	1426.9	417.6	1.14	0.26	1251.7	366.3
T5	1092.3	491.7	1.26	0.19	866.9	390.2
T6	1243.1	392.5	1.14	0.26	1090.5	344.3
T7	1025.5	258.6	0.72	0.33	1424.4	350.1
T8	2754.0	715.0	0.68	0.27	4049.9	1051.5
L1	1773.6	386.2	1.54	0.32	1151.7	250.8
L2	1118.0	97.7	1.26	0.19	887.3	77.5
L3	1152.3	132.2	0.72	0.33	1600.4	183.6
L4	2038.1	277.2	0.68	0.27	2997.3	407.7

Conclusion

L-PBF fabricated 304L stainless steel samples contained an order of magnitude higher concentration of oxygen than wrought 304L, and had high degrees of variation of concentration within the bulk of the material. Such variations led to inconsistent depths of penetration and an asymmetrical bead geometry with respect to the centerline by means of erratic surface tension driven (convective) fluid flow in the weld pool. The evolution of silicates in the molten weld pool of L-PBF samples potentially could act as nucleation sites within the weld. Irregular fluid flow and an increased number of nucleation sites contributed to significant changes in solidification behavior and microstructure near the root of the gas tungsten arc welded L-PBF 304L samples.

Acknowledgements

This investigation was conducted with the support of the Manufacturing and Materials Joining Innovation Center (Ma2JIC), a National Science Foundation – Industry/University Collaborative Research Center.

References

[1] J.C. Lippold and D.J. Kotecki, Welding Metallurgy and Weldability of Stainless Steels, Wiley, 2005.

[2] J.C. Lippold, “Weld Cracking Mechanisms in Austenitic Stainless Steels,” Proceedings of: Trends in Welding Research in the United States, ASM, pp. 209-241, 1982.

[3] J.C. Lippold, “Solidification Behavior and Cracking Susceptibility of Pulsed-Laser Welds in Austenitic Stainless Steels,” Welding Journal pp 129s –139s, June, 1994.

[4] S. Katayama, T. Fujimoto and A. Matsunawa, “Correlation among solidification process, microstructure, microsegregation and solidification cracking susceptibility in stainless steel weld metals, Transactions of JWRI, pp123, January, 1985.

[5] C.R. Heiple and J.R. Roper, “Mechanism for Minor Element Effect on GTA Fusion Zone Geometry,” Welding Journal pp 97s – 102s, April, 1982.

[6] C.R. Heiple, P. Burgardt, and J.R. Roper, “Control of GTA Weld Pool Shape,” Proceedings of: Trends in Welding Research in the United States, ASM, pp. 387-392, 1986.

[7] B. Pollard, “The Effects of Minor Elements on the Welding Characteristics of Stainless Steel,” Welding Journal pp 202s – 214s, September, 1988.

[8] S. A. David, J. M. Vitek, and T. Debroy, “Weld Pool Development during GTA and Laser Beam Welding of Type 304 Stainless Steel, Part II — Experimental Correlation,” pp. 510s–520s, December 1989.

[9] E. Folkhard, Welding Metallurgy of Stainless Steels, Springer-Verlag Wien New York, 1988.

[10] D.L. Olson, “Prediction of Austenitic Weld Metal Microstructure and Properties,” Welding Journal pp 281s – 295s, October, 1985.

[11] J.A. Brooks, “Solidification and Solid State Transformations of Austenitic Stainless Steel Welds,” Proceedings of: Trends in Welding Research in the United States, ASM, pp. 209-241, 1982.

[12] T. Iamboliev, S. Katayama and A. Matsunawa, “Interpretation of Phase Transformation in Austenitic Stainless Steel Welds,” Welding Journal pp 337s –347s, December, 2003.

[13] S.A. David, “Ferrite Morphology and Variations in Ferrite Content in Austenitic Stainless Steel Welds,” Welding Journal, pp 63s –71s, April, 1981.

[14] S. Kou. Welding Metallurgy, 2nd ed., Wiley, 2003.

[15] S. Katayama and A. Matsunawa, “Solidification Microstructure of Laser Welded Stainless Steels,” L.I.A. Vol. 44, ICALEO, pp 60-67, 1984.

[16] J.W. Elmer, S.M. Allen, and T.W. Eager, “Microstructural Development during Solidification of Stainless Steel Alloys,” Metallurgical Transactions A, V0l. 20A, pp 2117 – 2131, October, 1989.

[17] S. Kou and Y. Le, “The Effect of Quenching on the Solidification Structure and Transformation Behavior of Stainless Steel Welds,” Metallurgical Transactions A, V0l. 13A, pp 1141–1152, July, 1982.

[18] M. Yakout, M.A. Elbestawi, and S.C. Velduis, “On the characterization of stainless steel 316L parts produced by selective laser melting,” Int. Journal on Advanced Manufacturing Technology, Springer, November 2017.

[19] K. L. Johnson, T. M. Rodgers, O. D. Underwood, J. D. Madison, K. R. Ford, S. R. Whetten, D. J. Dagel, and J. E. Bishop, “Simulation and experimental comparison of the thermo-mechanical history and 3D microstructure evolution of 304L stainless steel tubes manufactured using LENS,” *Computational Mechanics*, vol. 61, no. 5, pp. 559–574, 2018.

[20] K.L. Johnson, T.M. Rodgers, O.D. Underwood, J.D. Madison, K.R. Ford, S.R. Whetten, D.J. Dagel and J.E. Bishop, “Simulation and experimental comparison of the thermo-mechanical

history and 3D microstructure evolution of 304L stainless steel tubes manufactured using LENS," Computational Mechanics, Springer, 61:559-574, 2018.

[21] S. B. Tate, "Laser Weldability of Type 21Cr-6Ni-9Mn Stainless Steel." Colorado School of Mines, Ph.D. Dissertation. 2015.

[22] D.J. Kotecki and T.A. Siewert, "WRC-1992 constitution diagram for stainless steel weld metals: a modification of the WRC-1988 diagram, Welding Journal, pp 171s –178s, May, 1992.